Vol.3, No.4, Page 922- 932, 2025 https://doi.org/10.59628/jast.v3i4.1649 ISSN 2958-9568 JAST

SUN PUBLISHER

مجلة جامعة صنعاء للعلوم التطبيقية والتكنولوجيا

Sana'a University Journal of Applied Sciences and Technology

https://journals.su.edu.ye/index.php/jast/

Zinc-Induced Effects on the Structural and Morphological Properties of Sn-Zn-In Triple Alloys: Insights from XRD, EDX, and SEM Analysis

Salam A.Q. ALarnoot[1, 2] *, A.H. Al-Hammadi[2] and Ahmed. M.A. Haider[2]

[1]**Department of Physics, Faculty of Science, Taiz University, Taiz, Yemen,**
[2]**Department of Physics, Faculty of Science, Sana'a University, Sana'a, Yemen**

*Corresponding author: salamalarnoot@gmail.com

Abstract

The primary objective of this study is to enhance the properties of Sn-In alloys by incorporating varying amounts of zinc (Zn) to develop alternative lead-free alloys suitable for electronic applications. The samples were synthesized using high-purity tin (Sn), indium (In), and zinc (Zn). Zn was added at different weight percentages (2, 4, 6, 8, and 10 wt. %) to the Sn-In base alloy. Structural analysis was performed using X-ray diffraction (XRD) to identify the phase formation and crystalline characteristics. Scanning electron microscopy (SEM) was employed to examine the microstructure, and energy-dispersive X-ray spectroscopy (EDX) was used to determine the elemental composition and phase distribution within the samples. The XRD results indicated that the Sn-Zn-In alloys exhibited a single-phase tetragonal structure. Increasing the Zn concentrations in the Sn matrix refined the grain size of the ternary Sn-Zn-In alloy. Additionally, Zn incorporation into the Sn-In binary alloy altered the intensity of the diffraction peaks and induced shifts in the (2θ) position, particularly in the 80Sn-10Zn-10In alloy. The calculated lattice parameters closely matched the standard values reported in JCPDS PDF# 04-0673, and no new phases were detected in the ternary systems. The SEM analysis revealed the presence of three distinct regions within the alloy microstructure: a gray region rich in β-Sn, a dark region corresponding to the indium-rich phase, and a white region representing the zinc-rich phase. The EDX spectra confirmed that the elemental composition of the Sn-Zn-In alloys closely matched the nominal ratios, indicating successful alloying and homogeneous elemental distribution.

Article Info

Keywords:
Sn-Zn-In alloy, Structural properties, (XRD), (SEM), (EDX).

Article History:
Received: 23-March-2025,
Revised: 21-May-2025,
Accepted: 5-July-2025,
Available online: 28 August 2025.

1. INTRODUCTION

Solders plays a crucial role in electronic packaging by providing both electrical conductivity and mechanical stability. Historically, the electronics industry has relied on eutectic or near-eutectic tin-lead (Sn-Pb) solder, with a melting point of 183 °C, owing to its excellent soldering performance and long-term reliability. However, over the past 15 years, a global initiative spearheaded by the European Union has aimed to eliminate the use of lead in electronic components, driven by increasing concerns regarding the environmental and health hazards posed by lead-containing solders. Lead is a well-known toxic element, with documented adverse effects on human health and the environment [1]. Consequently, significant efforts have been directed toward the development of lead-free solder alternatives that preserve essential attributes such as low melting temperature, cost-effectiveness, good wettability, and environmental compatibility [2]. Owing to the widespread use of solder materials in electronic interconnects, metal assemblies, and various components, ongoing research on soldering technologies remains vital [3]. Among lead-free alternatives, solder systems based on indium-tin (In-Sn) alloys have attracted considerable interest. These alloys offer advantages such as

low melting points and reduced mechanical stress during operation, which are attributed to their high ductility [4, 5]. Indium-based solders are particularly valued for aerospace and low-temperature applications, where they demonstrate excellent ductility and reliability under extended thermal cycling and cryogenic temperatures [6, 7]. For instance, the Sn-In eutectic alloy, which melts at 117 °C, is widely utilized in surface-mount technology (SMT) owing to its favorable thermal behavior. Similarly, Sn-Zn eutectic alloys, with a higher melting point of 198 °C, offer another promising option for specific applications [8, 9]. Despite the technical challenges, alloys incorporating low-melting-point elements such as Sn, Zn, and In have been extensively studied and are now widely used in commercial lead-free soldering processes [10]. Recent research has primarily focused on zinc-based solder alloys, which are often modified with additional elements to lower their melting points and improve their mechanical and physical properties [11–14]. Owing to their low cost, zinc-based alloys are increasingly being adopted across various sectors, including automotive, aerospace, and electronics, for use in die attachment, optical component assembly, and circuit module integration [15, 16]. Among these materials, Sn-Zn-In alloys have emerged as particularly promising owing to their unique combination of physical, thermal, and electrical properties. Their high electrical resistivity makes them suitable for solar cells and optoelectronic devices, where efficient charge transport is essential [17–19]. Furthermore, the tunable thermal and structural properties of these alloys make them highly effective for heat dissipation in electronic systems, thereby enhancing device reliability and operational stability [20, 21]. To optimize their performance, researchers have developing advanced techniques to precisely control the composition and microstructure of Sn-Zn-In alloys during manufacturing. These efforts have also focused on minimizing impurities, which can adversely affect the material properties. As a result, current studies aim to produce high-purity Sn-Zn-In alloys with controlled characteristics, enabling their integration into advanced technologies and broad industrial applications [22, 23]. The present study focuses on characterizing the structural properties of Sn-Zn-In alloys using X-ray diffraction (XRD), determining the elemental composition through energy-dispersive X-ray spectroscopy (EDX), and analyzing the surface morphology via scanning electron microscopy (SEM). These techniques provide comprehensive insights into the microstructural features of the alloy and are essential for assessing its suitability for advanced soldering and electronic applications.

2. EXPERIMENTAL PROCEDURES

High-purity tin (Sn), zinc (Zn), and indium (In) metals with a purity of approximately 99%, were used to prepare ternary Sn-Zn-In alloys. The alloys were synthesized by mixing these elements in varying weight percentages, specifically with indium contents of (18, 16, 14, 12, and 10 wt.%) and zinc contents of (2, 4, 6, 8, and 10 wt.%). Tin was maintained at a constant base composition of (80 wt.%) in all samples. These compositions were selected to investigate the structural properties of the Sn-Zn-In system using X-ray diffraction (XRD), scanning electron microscopy (SEM), and energy-dispersive X-ray spectroscopy (EDX). The ternary alloy compositions were prepared as follows: First, high-purity elemental materials were accurately weighed using a high-precision electronic balance (FISHER EMD, Model EMD-3100, Serial No: P0108837) with a sensitivity of approximately 1×10^{-4} g [5]. The elements were then grouped into five distinct sets according to the compositional ratios listed in Table 1. Each group of elements was thoroughly mixed to ensure uniformity and placed in Pyrex tubes. The alloying process was conducted by melting the metal constituents in a high-temperature electric furnace at 800 °C for approximately 3 h to ensure complete homogenization. After melting, the samples were allowed to solidify slowly inside the furnace to room temperature, promoting the full development of a constant scan rate of 0.02/1sec. SEM investigations were carried precipitated phases. After solidification, the samples were mechanically polished using a series of silicon carbide abrasive papers of increasing fineness. They were then cleaned using an acetone solution (CH_3COCH_3) to remove surface contaminants. Subsequently, the samples were cut into small sheets with a thickness of 0.6 mm, Finally, the samples were washed again in a solution of (CH_3COOH_3) in order to remove residual stress and defects induced during specimen formation [6–8]. and were investigated using XRD, SEM and EDX, respectively, on equilibrated alloys. The XRD analysis was performed using a Shimadzu EDX-720 diffract meter equipped with CuKα radiation (λ = 1.54056 Å). Data were collected over a 2θ range of 5–75° using an accelerating voltage of 40 kV and a tube current of 2 mA, with out using a JSM-6510LV scanning electron microscope (SEM). The SEM utilized secondary electron imaging, with a detector front screen biased at 200 V to attract low-energy secondary electrons, typically in the range of 3–5 eV. A standard SEM imaging process involves 1000-line scans to produce a 10 $\times$ 10 cm image, with the scanning cycle repeated at a frequency of 30 frames per second. Images were captured and recorded using a cathode ray tube equipped with a short-persistence phosphor to ensure a clear and stable visualization. The elemental composition and phase identification were further confirmed using EDX analysis integrated with the SEM system, allowing for qualitative and semi-quantitative analysis of the constituent elements in each alloy sample.

3. RESULTS AND DISCUSSION

Table 1. Ternary alloy groups.

Solder alloy WT%	Sn	In	Zn	Total
Sn-2Zn-In	80%	18%	2%	100%
Sn-4Zn-In	80%	16%	4%	100%
Sn-6Zn-In	80%	14%	6%	100%
Sn-8Zn-In	80%	12%	8%	100%
Sn-10Zn-In	80%	10%	10%	100%

Table 2. Represents X-ray diffraction patterns for (JCPDS-ICDD) (PDF# 04-0673) tetragonal phases.

No	2 θ	d (A^o)	I%	(hkl)
1	30.644	2.9150	100	(200)
2	32.018	2.7930	90	(101)
3	43.871	2.0620	34	(220)
4	44.902	2.0170	74	(211)
5	55.330	1.6590	17	(301)
6	62.538	1.4840	23	(112)
7	63.783	1.4580	13	(400)
8	64.576	1.4420	20	(321)

3.1. Structural analysis

Structural analysis was performed using X-ray diffraction (XRD) using Cu-Kα. Values of 2θ-Bragg's angle, d-spacing for the recorded peaks and the corresponding relative intensities (I/Io) (where Io is the maximum intensity peak). For each pattern and those obtained from (JCPDS-ICDD). To match the measured data from reference card no (PDF# 04-0673) listed in Table 2. The results of the XRD analysis of the Sn-Zn-In alloys are presented in Figures 1(a–e) and summarized in Tables (3-7). These findings were consistent with those reported by Athil AL-Ezzi et al. [24]. The most well-matched diffraction peaks for the synthesized samples are clearly identified in both the figures and the corresponding tables. The results showed that all prepared alloys exhibit a single-phase tetragonal crystal structure. The diffraction patterns shown in Figures 1(a–e) demonstrate that the addition of zinc to the Sn-In binary alloy leads to noticeable changes in peak intensities and causes shifts in the 2θ positions, as shown in Figure 1(e). As the ZN content increases, these shifts become more pronounced, which can be attributed to atomic migration and redistribution within the crystal lattice.

3.2. Particle size, dislocation density

The particle size (D) values for all Sn–x%Zn–In solder alloys were calculated using Scherrer equation Eq. (1) as follows [25]:

$$D = \frac{0.9\lambda}{\beta \cos\theta} \tag{1}$$

where, D is the size of the crystal particle, λ is the x-ray wavelength, β is the broadening of diffraction line measured at half its maximum intensity (radians) and θ is the Bragg angle. The calculated particle sizes are presented in Table 8. As observed in Table 7, the average particle size of the Sn–x%Zn–In alloys initially increases with Zn addition and then exhibits a sudden decrease. This behavior may be attributed to the homogeneous distribution and dynamic movement of atoms within the alloy matrix, which is influenced by the specific elemental composition. Evidence supporting this interpretation is provided by the EDX analysis of 80Sn–2Zn–18In and 80Sn–10Zn–10In, which demonstrate uniform elemental dispersion.

The variation in the average particle size of the Sn–x%Zn–In alloys as a function of Zn content was calculated and plotted, as illustrated in Figure 2. To further analyze the microstructural characteristics of these alloys, the dislocation density (δ) was evaluated. The dislocation density is a key parameter that indicates the degree of crystalline defects in an alloy and is defined as the total length of the dislocation lines per unit volume of the crystal. The dislocation density (δ) of the Sn–x%Zn–In alloys was calculated using Eq. (2) [26]:

$$\delta = \frac{1}{D^2} \tag{2}$$

where D is the average crystallite size, and the calculated values are summarized in Table 7, Fig.3 shows the relationship between dislocation density and Zn content. From both Figure 3 and Table 8, it is evident that the dislocation density increased with increasing Zn content. This trend can be attributed to the corresponding reduction in the particle size, which enhances the obstruction of dislocation motion within the crystal lattice. As illustrated in Figures 2 and 3, a decrease in the particle size

Table 3. X-ray diffraction patterns for 80Sn-2Zn-18In alloy.

No	2θ	d (A^o)	hkl	I%	FWHM	Crystallite size D (nm)	$\delta = \frac{1}{D^2}$ ($\times 10^{-3}$ nm)
1	30.736	2.9065	(200)	4.8	0.145	51.69387333	0.000374216
2	31.78	2.8134	(101)	100	0.291	49.9961704	0.000400061
3	43.784	2.0659	(220)	61.5	0.178	36.28872351	0.000759376
4	44.781	2.0222	(211)	34.6	0.196	35.48083114	0.000794351
5	55.405	1.6122	(301)	83.7	0.155	28.67726047	0.001215975
6	62.481	1.4852	(112)	18.3	0.242	25.42968222	0.001546391
7	65.601	1.4219	(400)	11.4	0.0.252	24.22025839	0.001704678
8	65.801	1.4181	(321)	26.6	0.222	24.1465894	0.001715096
Average						**34.49167361**	**0.001063767**

Table 4. X-ray diffraction patterns for 80Sn-4Zn-16In alloy.

No	2θ	d (A^o)	hkl	I%	FWHM	Crystallite size D (nm)	$\delta = \frac{1}{D^2}$ ($\times 10^{-3}$ nm)
1	30.636	2.9157	(200)	0.4	0.116	51.86246953	0.000371786
2	32.56	2.7478	(101)	100	0.34	48.79805885	0.000419947
3	44.96	2.0145	(211)	17.5	0.248	35.3394467	0.00080072
4	55.336	1.5928	(301)	22.5	0.2	28.71295761	0.001212953
5	66.5	1.4049	(400)	19.2	0.159	23.89262153	0.001751751
6	67.92	1.3789	(321)	12	0.325	23.39317127	0.00182735
Average						**35.33312092**	**0.001064085**

Table 5. X-ray diffraction patterns for 80Sn-6Zn-14In alloy.

No	2θ	d (A^o)	hkl	I%	FWHM	Crystallite size D (nm)	$\delta = \frac{1}{D^2}$ ($\times 10^{-3}$ nm)
1	30.98	2.8842	(200)	18.8	0.25	51.28705382	0.000380176
2	32.479	2.7544	(101)	100	0.177	48.91977536	0.00041786
3	35.881	2.5007	(002)	6.3	0.255	44.28175186	0.000509977
4	44.839	2.0197	(220)	27.3	0.174	35.43489215	0.000796412
5	45.44	1.9943	(211)	82.3	0.172	34.96621835	0.000817905
6	55.98	1.6413	(213)	9.8	0.13	28.38267046	0.001241348
7	57.761	1.5948	(301)	19.9	0.212	27.50763801	0.00132158
8	63.199	1.4701	(112)	19.3	0.153	25.14064253	0.001582149
9	65.301	1.4277	(400)	10.5	0.185	24.33142042	0.001689138
10	66.441	1.406	(321)	16.1	0.174	23.91392558	0.001748631
Average						**34.41659885**	**0.001050517**

leads to an increase in the number of particle boundaries within the alloy. These particle boundaries serve as effective barriers to the movement of dislocations and other lattice imperfections, thereby contributing to an increase in dislocation density. For example, Table 8 shows that Sample 5, which has a particle size of (31.57), exhibits a dislocation density of (1.23). In contrast, when the particle size increased, the density of the particle boundaries decreases, allowing dislocations to move more freely, resulting in fewer crystalline defects. This trend is evident in sample 4, where a particle size of (36.17) corresponds to a significantly lower dislocation density of (0.97), as reported in Table 8.

Table 6. X-ray diffraction patterns for 80Sn-8Zn-12In alloy.

No	2θ	d (A^o)	hkl	I%	FWHM	Crystallite size D (nm)	$\delta = \frac{1}{D^2}$ ($\times 10^{-3}$ nm)
1	31.02	2.8806	(200)	8.4	0.261	51.22056492	0.000381163
2	32.539	2.7495	(101)	100	0.195	48.82940788	0.000419408
3	35.922	2.4979	(002)	4.1	0.215	44.23085015	0.000511151
4	44.899	2.0171	(220)	15.4	0.19	35.38742481	0.00079855
5	45.5	1.9919	(211)	17	0.167	34.91998879	0.000820072
6	57.859	1.5924	(301)	41.7	0.171	27.46088891	0.001326083
7	66.519	1.4045	(400)	23.1	0.186	23.88580549	0.001752751
8	67.8	1.3811	(321)	9	0.171	23.43450696	0.001820909
Average						**36.1717974**	**0.00097876**

Table 7. X-ray diffraction patterns for 80Sn-10Zn-10In alloy.

No	2θ	d (A^o)	hkl	I%	FWHM	Crystallite size D (nm)	$\delta = \frac{1}{D^2}$ ($\times 10^{-3}$ nm)
1	32.799	2.7283	(101)	100	0.269	48.44239703	0.000426137
2	45.438	1.9944	(211)	4.2	0.433	34.9678495	0.000817828
3	58.36	1.5799	(201)	5.8	0.493	27.22536852	0.001349126
4	66.642	1.4022	(400)	11.6	0.22	23.8417324	0.001759237
5	68.02	1.3771	(321)	15.5	0.179	23.35871422	0.001832745
Average						**31.56721233**	**0.001237015**

Table 8. The Particle size (D) and Dislocation density Sn-x%Zn-In alloys.

Samples wt.%	Particle size (D) (nm)	Dislocation density (δ) $\times 10^{-3}$ (nm)$^{-2}$
Sn-2%Zn-In	34.51	1.06
Sn-4%Zn-In	35.33	1.07
Sn-6%Zn-In	34.41	1.05
Sn-8%Zn-In	36.17	0.97
Sn-10%Zn-In	31.57	1.23

3.3. The X-ray density (D_x) and bulk density (D_b)

Due to the expansion along the a- and c-axes upon the addition of Zn, a slight Variations in the axial ratio (c/a) was observed. The estimated lattice parameters a and c are listed in Table 8. The highest axial ratio, (c/a) = 0.586, was recorded for the 2 wt.% Zn, which can be attributed to the elongation of the c-axis and the contraction of the a-axis. This structural change resulted in a reduction in the unit cell volume to 55.618 (A^o)^3, as also shown in Table 9. The unit cell volume (V_c) was calculated using Equation Eq. (3) [27]:

$$V_c = a^2.c \tag{3}$$

Figures 4 and 5 show that the density of the Sn-6%Zn-In sample lies within the range of (7.942–7.9584 g/cm^3). This variation is likely due to the presence of intermetallic particles within the matrix, which may have resulted from grain boundary segregation or partial dissolution. The density values reported in Table 9 closely match the standard density for tetragonal phases, according to the JCPDS-ICDD database (PDF# 04-0673). Similarly, the bulk density was ranged between 6.524 and 7.826 g/cm^3.

3.4. EDX analysis

Energy-dispersive X-ray spectroscopy (EDX) analysis confirmed the presence of the constituent elements Sn, Zn, and In in the examined alloys. As illustrated in Figures 6 (a) and 6 (b), the corresponding weight and atomic percentages are presented in the inset tables. The chemical composition of the Sn-Zn-In alloys, as determined by EDX, closely matches the nominal compositions used during synthesis. The representative EDX spectra validate the successful alloying process, demonstrating a strong correlation between the measured elemental ratios and the intended stoichiometric proportions. The elemental composition obtained from the EDX analysis was found to be in agreement with the phase structure identified by XRD. The atomic ratios derived from EDX closely matched the stoichiometric proportions expected

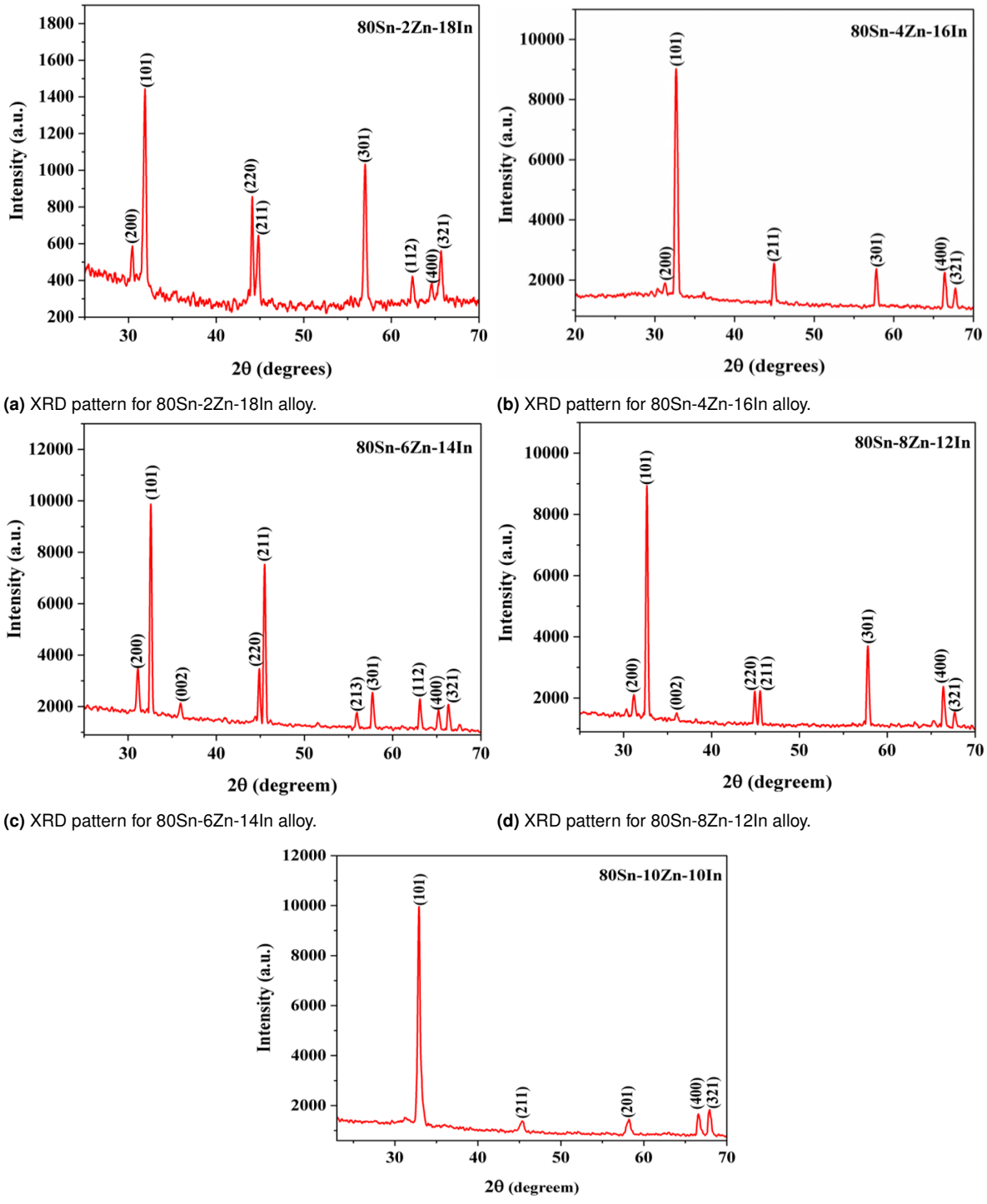

(a) XRD pattern for 80Sn-2Zn-18In alloy.

(b) XRD pattern for 80Sn-4Zn-16In alloy.

(c) XRD pattern for 80Sn-6Zn-14In alloy.

(d) XRD pattern for 80Sn-8Zn-12In alloy.

(e) XRD pattern for 80Sn-10Zn-10In alloy.

Figure 1

Table 9. The X-ray density (D_x) and bulk density (D_b).

Samples wt.%	Zn addition %	a (nm)	c (nm)	(c/a) (nm)	Cell volume $(A^o)^3$	D_x (gm/cm^3)	D_b (gm/cm^3)
Sn-2%Zn-18In	2	0.5564	0.3260	0.586	58.597	7.6955	7.423
Sn-4%Zn-16In	4	0.5528	0.3166	0.572	56.173	7.9584	6.622
Sn-6%Zn-14In	6	0.5783	0.3131	0.541	60.795	7.2942	6.524
Sn-8%Zn-12In	8	0.5525	0.3169	0.573	56.165	7.8247	7.826
Sn-10%Zn-10In	10	0.5526	0.3137	0.576	55.618	7.836	7.817

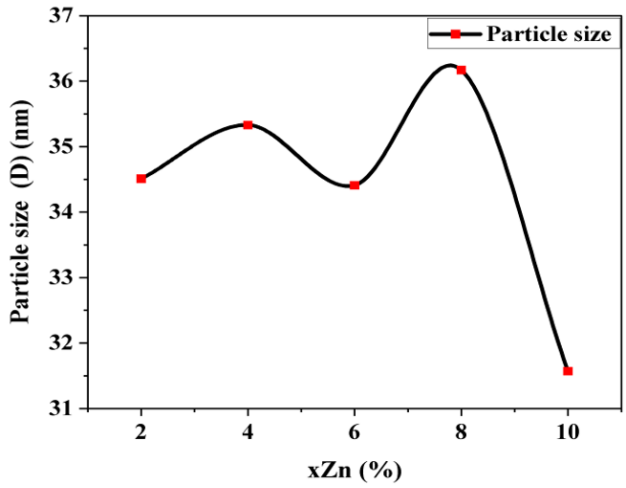

Figure 2. The variation in particle size values of Sn-x%Zn-In with Zn content.

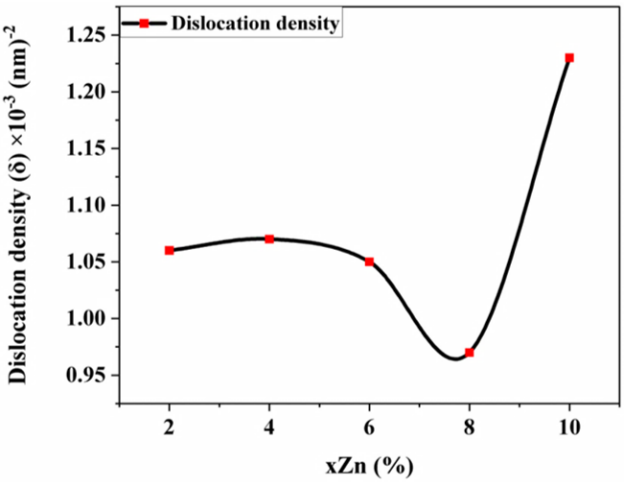

Figure 3. The variation in values dislocation density values of Sn-x%Zn-In with Zn content.

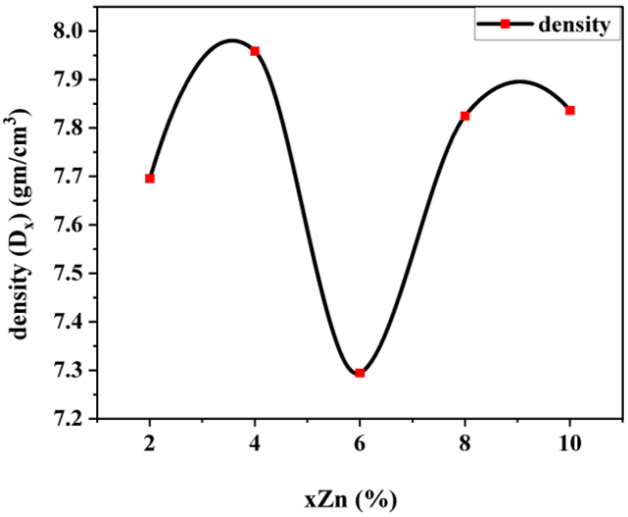

Figure 4. The X-ray density (D_x) of Sn-x%Zn-In with Zn content.

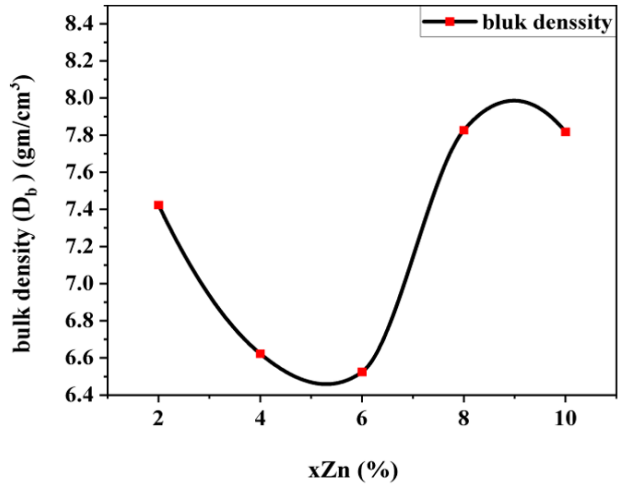

Figure 5. The bulk density (D_b) of Sn-x%Zn-In with Zn content.

for the crystalline phase detected, suggesting a consistent distribution of elements within the analyzed region. This correlation reinforces the reliability of the phase identification and confirms the homogeneity of the alloy system at both the structural and compositional levels. A comparative analysis between the first and fifth samples reveals a significantly higher zinc content in the fifth sample. This is demonstrated by the denser atomic packing observed in the (101) crystallographic plane, as indicated by the increased relative intensity of the X-ray diffraction for this plane in the fifth sample compared to the first.

3.5. SEM ANALYSIS

In Figure 7 (a–e), scanning electron microscopy (SEM) images illustrate the microstructure of the Sn-Zn-In alloy system at varying zinc concentrations. Microstructural analysis revealed the presence of three distinct phases: a β-Sn-rich region appearing gray, an indium-rich phase characterized by a dark black contrast, and a zinc-rich phase that appears white. In Figure 7(a), the microstructure of the Sn-2Zn-In alloy reveals a dispersed spherical morphology of indium-rich phases randomly distributed throughout the matrix. These dark black regions are embedded within a tin-rich matrix, along with a few small zinc particles. This distribution is likely attributable to the high Sn content of the alloy [28]. Figure 7 (b) depicts the Sn-4Zn-In alloy, where the zinc-rich phase appears as large, white spherical precipitates dispersed within the tin-rich gray matrix. The morphology suggests that the limited diffusion time during furnace processing may have led to the precipitation of zinc in a spherical form. As shown in Figure 7 (c), the Sn-6Zn-In alloy exhibits a dendritic microstructure with small, homogeneously distributed zinc-rich phase remained in the form of dispersed dark-black spheres. The zinc-rich phase appeared homogeneously embedded in the gray tin matrix, predominantly in the form of fine platelets rather

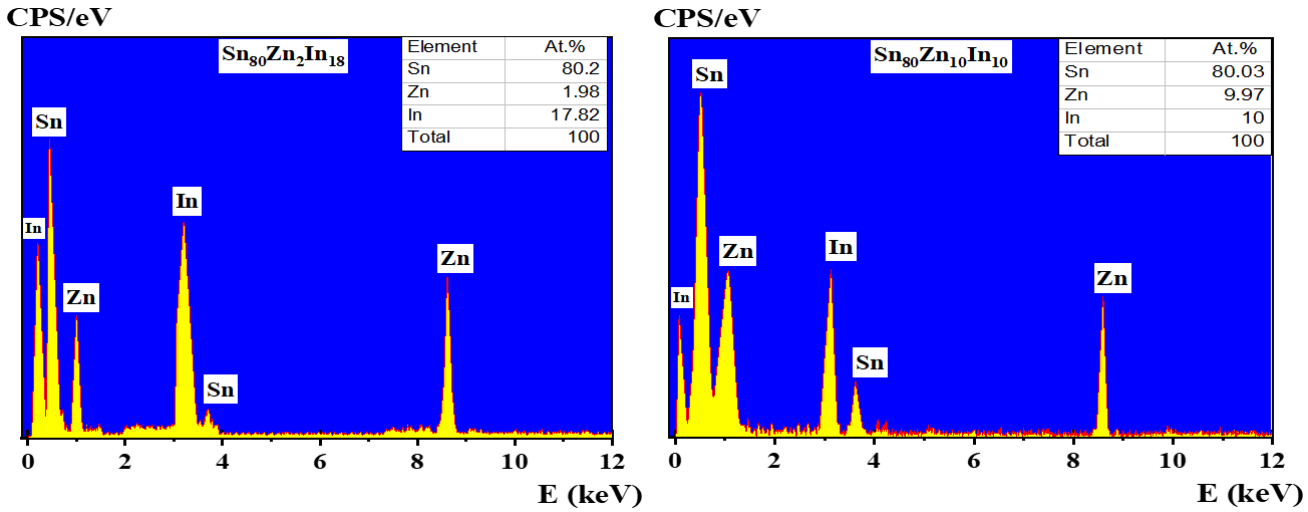

Figure 6. EDX of the elements (Sn, Zn and In) in (a) 80Sn-2Zn-18In- and (b) 80Sn-10Zn-10In alloys.

than spheres. This transformation could be attributed to globules within the tin matrix. Dark black regions, representing the indium-rich phase, are also evident. These features likely result from temperature gradients and rapid cooling rates during solidification. Figure 7 (d) shows the microstructure of the Sn-8Zn-In alloy, highlighting a well-defined tin-rich matrix in gray, with zinc-rich phases forming scattered white dendritic structures. A few small, dark black indium-rich spheres were observed along the grain boundaries. The apparent homogeneity of the zinc phase within the matrix may be due to the slower cooling rates, which facilitate phase diffusion and distribution. Finally, Figure 7 (e) illustrates the Sn-10Zn-In alloy, in which the indium-rich grain refinement and an increased number and size of zinc-rich features, promoting plate formation over spheroidal morphology.

In Figure 8. The particle size distribution exhibits. The distribution curve derived from the SEM images confirmed the uniformity of the particle sizes, indicating that the synthesis process was effective in controlling the grain nucleation. This uniformity is attributed to the presence of Zn, which plays a critical role in suppressing grain growth during alloy formation. SEM analysis provided a direct observation of the particle size distribution, revealing the overall morphology and agglomeration state of the Sn–x%Zn–In alloy samples. The XRD results revealed the particle size within those particles. In all samples, the average particle size observed via SEM was significantly larger than that calculated from XRD, indicating that the particles were polycrystalline in nature. This difference suggests that each particle consists of multiple crystallites, and consequently, the refinement of particle size as determined by XRD, is consistent with the increased SEM-measured particle size.

4. CONCLUSIONS

In this study, a series of Sn-In-Zn ternary alloys was successfully developed to enhance their structural and microstructural properties for use in lead-free electronic applications. The addition of zinc at various concentrations (2–10 wt.%) to the Sn-In base alloy resulted in noticeable improvements without the formation of any secondary or intermetallic phases. X-ray diffraction analysis confirmed the presence of a stable single-phase tetragonal structure across all compositions, with slight shifts in the diffraction peak positions and grain refinement with increasing Zn content. An alloy with 10 wt.% Zn exhibited the most significant structural shifts, suggesting enhanced atomic interactions within the lattice Ane as the structural analysis of Sn–x%Zn–In solder alloys demonstrates that increasing Zn content alters atomic mobility and defect structures by inducing lattice distortions, modifying dislocation density, particle size, and crystallographic parameters, as confirmed by XRD and density measurements. Microstructural examination using SEM revealed well-defined and distinct phases corresponding to Sn-, In-, and Zn-rich regions, indicating a good distribution of the alloying elements. Furthermore, EDX analysis verified that the elemental compositions closely matched the intended stoichiometries, confirming the effectiveness of the alloying process and homogeneity of the resulting materials. Overall, the results demonstrate that the addition of Zn not only stabilizes the crystal structure but also improves the uniformity and integrity of the microstructure, making Sn-In-Zn alloys promising candidates for reliable, lead-free solder materials in advanced microelectronic applications.

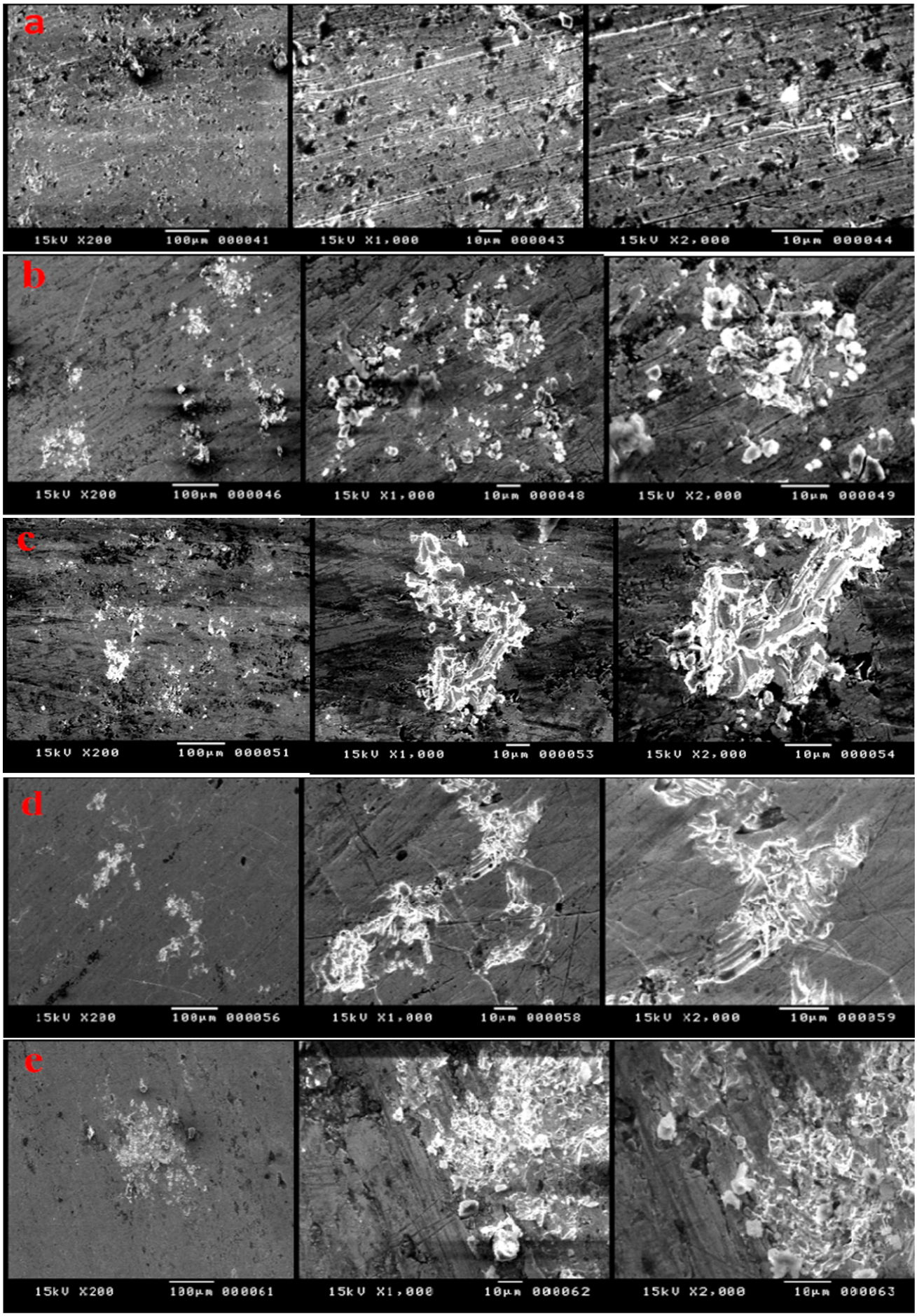

Figure 7. (a-e).SEM images of Sn-x%Zn-In.

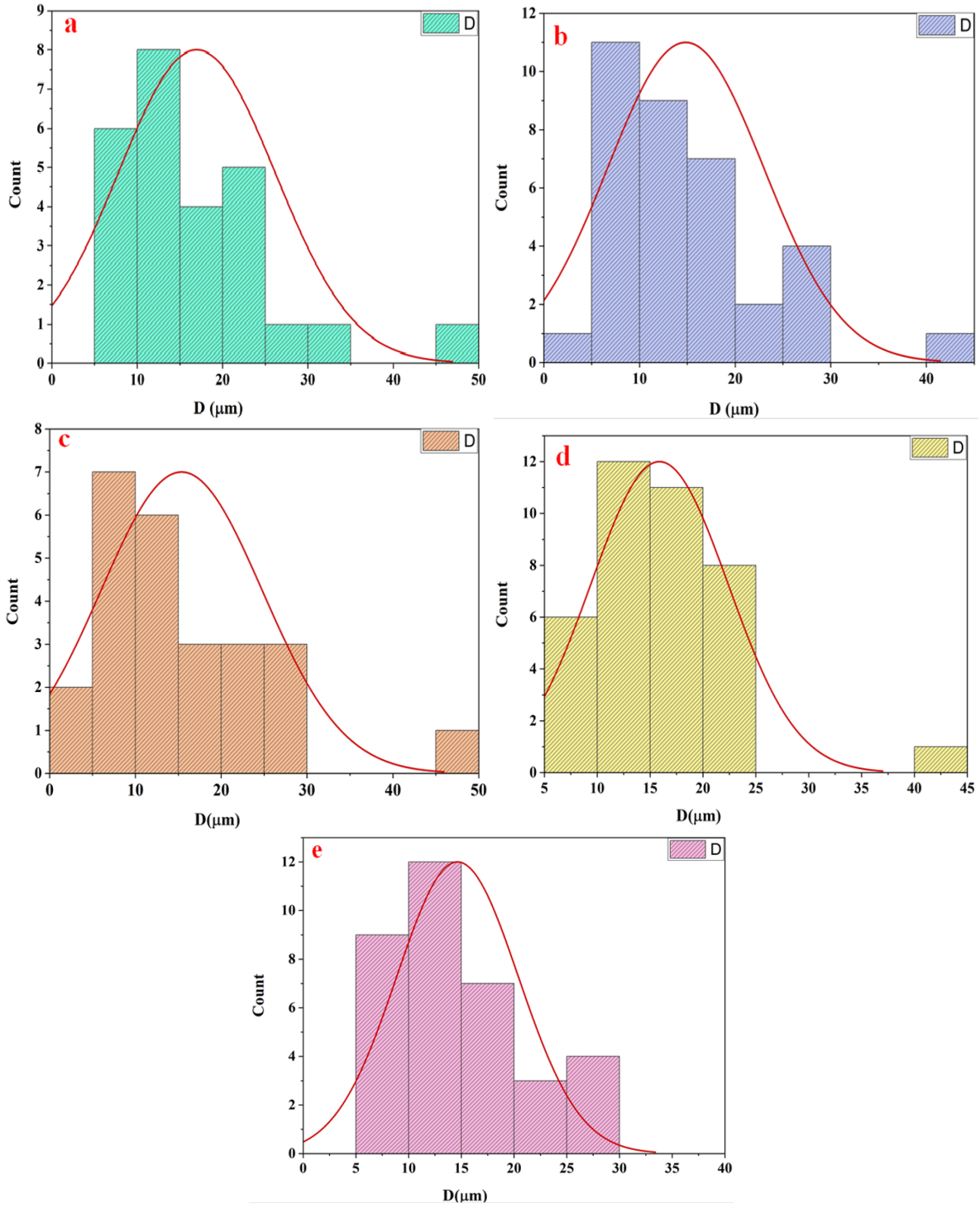

Figure 8. particle size distribution

REFERENCES

[1] B. R. Allenby and J. P. Ciccarelli, "An assessment of the use of lead in electronic assembly," in *Proceedings of Surface Mount International Conference,* (1992), pp. 1–28.

[2] H. Y. Zahran *et al*., "Effect of bi content on the microstructure and mechanical performance of sn-1ag-0.5 cu solder alloy," Crystals **11**, 314 (2021).

[3] E. Öztürk, "Mechanical and microstructural properties of in, ag, al doped lead-free sn-zn solder alloy systems," Unkn. J. **22**, 477–485 (2022).

[4] R. W. Chang and P. F. McCluskey, "Reliability assessment of indium solder for low temperature electronic packaging," Cryogenics **49**, 630–634 (2009).

[5] M. Plötner, B. Donat, and A. Benke, "Deformation properties of indium-based solders at 294 and 77 k," Cryogenics **31**, 159–162 (1991).

[6] M. Deshpande, R. Chaudhari, P. R. Narayanan, and H. Kale, "Evaluation of shear properties of indium solder alloys for cryogenic applications," J. Mater. Eng. Perform. **30**, 7958–7966 (2021).

[7] C. D. Tudryn, "Solder joint fatigue study under low temperature martian conditions," in *Proceedings of the IEEE Aerospace Conference,* vol. 9 (Big Sky, MT, USA, 2006), pp. 4–11.

[8] S. S. Murugan *et al*., "Mechanical properties of materials: definition, testing and application," Int. J. Mod. Stud. Mech. Eng. (IJMSME) **6**, 28–38 (2020).

[9] J. R. Davis *et al*., *Tensile Testing* (ASM International, 2004).

[10] A. Debski, B. Onderka, W. Gasior, and T. Gancarz, "Unknown title," Arch. Metall. Mater. **62**, 1945–1955 (2017).

[11] A. Haque, B. H. Lim, A. S. M. A. Haseeb, and H. H. Masjuki, "Die attach properties of zn-al-mg-ga-based high-temperature lead-free solder on a cu lead-frame," J. Mater. Sci. Mater. Electron. **23**, 115–123 (2012).

[12] Y. Takaku, L. Felicia, and I. Ohnuma, "Interfacial reaction between cu substrates and zn-al base high-temperature pb-free solders," J. Electron. Mater. **37**, 314–323 (2008).

[13] S. Alibabaie and R. Mahmudi, "Microstructure and creep characteristics of zn-3cu-xal ultra high-temperature lead-free solders," Mater. Des. **39**, 397–403 (2012).

[14] G. Zeng, S. McDonald, and K. Nogita, "Development of high-temperature solders: Review," Microelectron. Reliab. **52**, 1306–1322 (2012).

[15] L. Zhang, S. Xue, L. Gao, *et al*., "Effects of rare earths on properties and microstructures of lead-free solder alloys," J. Mater. Sci. Mater. Electron. **20**, 685–694 (2009).

[16] S. Wang, H. Zhou, and Y. Kang, "The influence of rare earth elements on microstructure and properties of 6061 aluminum alloy vacuum-brazed joints," J. Alloy. Compd. **352**, 79–83 (2003).

[17] C. M. Mendez *et al*., "Electrochemical behavior of sn-zn alloys with different grain structures in chloride-containing solutions," Arab. J. Chem. **11**, 1084–1096 (2018).

[18] S. E. A. Negm, A. S. A. Moghny, and S. I. Ahmad, "Investigation of thermal and mechanical properties of sn-zn and sn-zn-bi near-eutectic solder alloys," Results Mater. **15**, 100316 (2022).

[19] Žaneta Gerhátová *et al*., "Microstructure and corrosion behavior of sn–zn alloys," Materials **15**, 7210 (2022).

[20] J.-E. Lee *et al*., "Thermal properties and phase stability of zn-sn and zn-in alloys as high-temperature lead-free solders," Mater. Trans. **48**, 584–593 (2007).

[21] Z. Moser *et al*., "The snzn (tin-zinc) system," Bull. Alloy. Phase Diagrams **6**, 330–334 (1985).

[22] B.-J. Lee, "Thermodynamic assessments of the sn-zn and in-zn binary systems," Calphad **20**, 471–480 (1996).

[23] J. Pstruś, "Surface tension and density of liquid in–sn–zn alloys," Appl. Surf. Sci. **265**, 50–59 (2013).

[24] A. Al-Hammadi, F. Ghailan, and S. AL-Aghbari, "Investigation of the structural and mechanical properties of ((82-x) sn xcu -18 in) % alloy with x= 1, 2, 3, 4 and 5," Sana'a Univ. J. Appl. Sci. Technol. **1**, 225–233 (2023).

[25] A. Al-Hammadi, I. G. Loqman, and R. AL-Hdhrami, "Mechanical properties of the (81sn–xcu–(19-x) in) % alloys with x=1, 2, 3, 4, and 5," Sana'a Univ. J. Appl. Sci. Technol. **1**, 189–198 (2023).

[26] S. AlSowidy, A. Aljarbani, and M. Gumaan, "Microstructural and creep characterization of sn-0.7 cu and sn-0.7 cu xbi lead-free solders for low cost electronics," Results Mater. **16**, 100319 (2022).

[27] A. AL-HAMMADI, F. Ghailan, and F. A. Hulaiqah, "Effect of melting at different temperatures on the structure and mechanical properties of solder alloy (sn ag-in)," Albaydha Univ. J. **3**, 161–181 (2021).

[28] A. AL-Ezzi, A. AL-Bawee, F. Dawood, and A. A. Shehab, "Effect of bismuth addition on physical properties of sn-zn lead-free solder alloy," J. Electron. Mater. **48**, 8089–8095 (2019).